Int. J. Heat Mass Transfer. Vol. 35, No. 5, pp. 1307–1324, 1992
Printed in Great Britain

0017–9310/92 $5.00 + 0.00

Numerical analysis of convecting, vaporizing fuel droplet with variable properties

C. H. CHIANG, M. S. RAJU† and W. A. SIRIGNANO
Department of Mechanical and Aerospace Engineering, University of California, Irvine, CA 92717, U.S.A.

(*Received* 20 *June* 1989 *and in final form* 18 *February* 1991)

Abstract—Detailed analysis of a cold fuel droplet suddenly injected into a hot gas stream is examined. The effects of variable thermophysical properties, transient heating and internal circulation of liquid, deceleration of the flow due to the drag of the droplet, boundary-layer blowing, and moving interface are included. Several parametric studies are performed by changing the following quantities: initial droplet temperature, ambient temperature, initial Reynolds number, fuel type, and droplet heating model. The results show that for higher transfer numbers, the vaporization rate is larger and the drag coefficient is significantly reduced mainly due to a large reduction in friction drag. For lower transfer numbers, the boundary-layer blowing effect is weaker and the drag coefficient is dominated by the Reynolds number only. The results also indicate that the constant-property calculation overestimates the drag coefficient.

1. INTRODUCTION

MANY PRACTICAL combustion devices involve direct injection of liquid fuel into the combustor. The atomizer breaks the liquid fuel into a large number of droplets. The droplets subsequently vaporize in the convective gas stream to form the air–fuel mixture. Typically, the fuel is of sufficiently low volatility that vaporization is an important controlling factor in the estimation of combustion rates. In the combustor design, it is desirable to analyze the trajectory, heating and vaporizing history of a droplet in order to determine the combustor dimensions and predict combustor performance, stability and pollutant emissions. Therefore, a detailed investigation of local as well as overall behavior of the droplet vaporization process is very important in the design of rocket, ramjet, gas turbine combustors and furnaces. The results obtained from a single droplet computation can be provided as the fundamental input for the spray calculation.

The early theoretical treatment of transport processes of a moving droplet was reviewed by Clift *et al.* [1]. However, the consideration of vaporization was not included in their literature review.

Law [2] and others before him provided an 'infinite conductivity' model for the liquid phase by assuming rapid internal mixing. The droplet temperature is spatially uniform but varying with time. The model provides an easy way to evaluate vaporization but is not realistic in practical situations. The infinite conductivity assumption is relaxed in the conduction limit model by Law and Sirignano [3]. The internal circulation is not considered in this spherically-symmetric model.

For a vaporizing droplet in a convective flow field, many experimental researchers suggested that the vaporization rate for an isolated droplet in a stagnant environment be modified by an empirical correction factor such as in the Ranz–Marshall correlation. By using theoretical analysis, Sirignano [4] indicated that a correlation of the Ranz–Marshall type can yield inaccurate results owing to the inaccurate dependence upon the transfer number.

The earlier droplet models for both gas and liquid phases by Prakash and Sirignano [5], Lara-Urbaneja and Sirignano [6], and Tong and Sirignano [7] considered the transient heating and internal motion effects of the liquid phase along with quasi-steady and constant physical property assumptions for the gas phase. Through the use of approximate similar solutions for the boundary layer around the gas/liquid interface, the complex flow field can be approximated by a one-dimensional treatment. The significant contributions from the above simplified droplet models are summarized in Sirignano [8]. In fact, their analysis is strictly correct only at very high Reynolds number flow due to the boundary layer assumption. The models neglect the recirculating wake near the rear stagnation point. Hence, the results of simplified models are of doubtful accuracy, although the contribution of shear stress or heat flux is not significant in the wake region. In addition, the pressure drag cannot be calculated due to the potential flow assumption in the outer region. The studies from the above researchers all indicated that the transient heating has a substantial influence on the interface transport coefficients. The flow field, therefore, must be treated as a transient problem until the droplet reaches its boiling temperature.

On account of the assumptions of the simplified models, the 'exact solution' of the complete set of unsteady Navier–Stokes, energy and species equa-

† Present address: Sverdrup Technology, Cleveland, OH 44130, U.S.A.

NOMENCLATURE

a instantaneous radius, a'/a'_0
B_H effective heat transfer number, $C'_{p_{g,film}}(T'_\infty - T'_S)(1-Q'_l/Q'_g)/L'_S$
B_M mass transfer number, $(Y_{f,S}-Y_{f,\infty})/(1-Y_{f,S})$
C_D total drag coefficient, $C_p+C_f+C_t$
$C_{D,f}$ friction drag coefficient, $2F'_f/(\rho'_{g,\infty}U'^2_\infty \pi a'^2)$
$C_{D,p}$ pressure drag coefficient, $2F'_p/(\rho'_{g,\infty}U'^2_\infty \pi a'^2)$
$C_{D,t}$ thrust drag coefficient, $2F'_t/(\rho'_{g,\infty}U'^2_\infty \pi a'^2)$
C_{p_g} specific heat of gas phase, $C'_{p_g}/C'_{p_{g,\infty}}$
C_{p_l} specific heat of liquid phase, $C'_{p_l}/C'_{p_{l,0}} = 1$
C_1, C_2 coefficients in Clasius–Clapeyron relationship
D_g mass diffusivity of gas phase, $D'_g/D'_{g,\infty}$
F force, $F'/(U'^2_{\infty,0}a'^2_0\rho'_{g,\infty})$
h enthalpy, $h'/(C'_{p_{g,\infty}}T'_{g,\infty})$
L latent heat of vaporization, $L'/(T'_\infty C'_{p_{l,0}})$
Le_g gas phase Lewis number, $\rho'_{g,\infty}D'_{g,\infty}C'_{p_{g,\infty}}/\kappa'_{\infty,0}$
M equivalent molecular weight, M'/M'_∞
p pressure, $(p'-p'_\infty)/(\rho'_{g,\infty}U'^2_{\infty,0})$
Pe_g gas phase Peclet number, $Re_g\,Pr_g$
Pe_l liquid phase Peclet number, $Re_l\,Pr_l$
Pr_g gas phase Prandtl number, $\mu'_{g,\infty}C'_{p_{g,\infty}}/\kappa'_{g,\infty}$
Pr_l liquid phase Prandtl number, $\mu'_{l,0}C'_{p_{l,0}}/\kappa'_{l,0}$
Q' heat flux
r radial coordinate, r'/a'_0
R gas constant, $R^0T'_\infty/(U'^2_{\infty,0}M'_\infty)$
R^0 universal gas constant
Re_g gas phase Reynolds number, $a'_0U'_{\infty,0}\rho'_{g,\infty}/\mu'_{g,\infty}$
Re_l liquid phase Reynolds number, $a'_0U'_{\infty,0}\rho'_{l,0}/\mu'_{l,0}$
Re_m modified gas phase Reynolds number, $a'U'_\infty\rho'_{g,\infty}/\mu'_{film}$
Sc_g gas phase Schmidt number, Pr_g/Le_g
T temperature, T'/T'_∞
t' time
U_∞ instantaneous free-stream velocity, $U'_\infty/U'_{\infty,0}$
V velocity, $V'/U'_{\infty,0}$
Y_i mass fraction
z axial coordinate, z'/a'_0.

Greek symbols
θ angular coordinate
κ_g conductivity of gas phase, $\kappa'_g/\kappa'_{g,\infty}$
κ_l conductivity of liquid phase, $\kappa'_l/\kappa'_{l,0} = 1$
μ_g viscosity of gas phase, $\mu'_g/\mu'_{g,\infty}$
μ_l viscosity of liquid phase, $\mu'_l/\mu'_{l,0}$
ξ, η generalized coordinates
ρ_g density of gas phase, $\rho'_g/\rho'_{g,\infty}$
ρ_l density of liquid phase, $\rho'_l/\rho'_{l,0} = 1$
τ_{Hg} gas-thermal-diffusion time, $t'\kappa'_{g,\infty}/(a'^2_0\rho'_{g,\infty}C'_{p_{g,\infty}})$
τ_{Hl} liquid-thermal-diffusion time, $t'\kappa'_{l,0}/(a'^2_0\rho'_{l,0}C'_{p_{l,0}})$
τ_{Hg} gas-hydrodynamic-diffusion time, $t'\mu'_{g,\infty}/(a'^2_0\rho'_{g,\infty})$
τ_{Hl} liquid-hydrodynamic-diffusion time, $t'\mu'_{l,0}/(a'^2_0\rho'_{l,0})$
τ_S gas-species-diffusion time, $t'D'_{g,\infty}/(a'^2_0)$
χ mole fraction
ψ stream function, $\psi'/a'^2_0U'_{\infty,0}$
ω vorticity, $\omega'a'_0/U'_{\infty,0}$.

Subscripts
av spatial average
d droplet
f fuel
film film conditions (average of ambient and surface conditions)
g gas phase
l liquid phase
n normal direction
r radial direction
re relative
s at the droplet surface
v volumetric average
wet wet-bulb temperature
z axial direction
0 initial conditions
θ tangential direction
∞ free stream conditions.

Superscripts
′ dimensional quantity
* estimate at the new time step.

tions with a minimal amount of approximation is highly desirable. The 'exact solution' is expected to bring more new, useful and detailed information that characterizes the droplet behavior. Also, the 'exact solution' can be used as a basis for comparison with simplified models. The droplet research which solves the whole gas/liquid transport equations is discussed in the following literature review.

Dwyer and Sanders [9–11] attacked this unsteady problem by assuming uniform gaseous density and formulated the flow field by a stream function and vorticity approach. Their results indicated that the drag coefficient reduction by boundary layer blowing is more than the drag increase due to the decrease in Reynolds number (via the deceleration of the droplet). Hence they predicted a drag coefficient decrease with time. The variable density case has been studied by Patnaik *et al.* [12], who found that the trend for

the drag coefficient is generally the same but more dramatic than in the uniform density case. Ayyaswamy and his research associates [13–15] studied the condensation phenomena of a moving droplet over a range of Reynolds numbers by both singular perturbation techniques and numerical methods. The same quasi-steady assumptions for gas and liquid transport processes (except liquid phase heating) and constant property assumptions were employed. Their results showed some interesting relationships between drag coefficient and surface normal velocity. For droplets in a very high temperature and pressure environment, these assumptions and results become questionable.

Haywood *et al.* [16] considered a droplet evaporating in an environment at ambient temperature and pressure too low to be characteristic of combustors. Their variable property calculation showed that the drag coefficient increases during the droplet lifetime. They explained that although the net effects of variable properties and surface blowing tend to decrease the drag, the increase of pressure drag is more remarkable. They also presented a steady-state correlation for the total drag, Nusselt and Sherwood numbers and found that the correlation is applicable in some complex hydrocarbon calculations. It is not very clear whether the correlation is applicable to the high transfer number cases with noticeable mass transfer occurring at the interface.

The purpose of the present study is to solve numerically the equations governing the exchange of momentum, mass and energy between a vaporizing droplet and the convective gas environment with high values of transfer number, to analyze the local as well as overall behavior of the droplet, to study the important effects due to variable properties and to Reynolds and transfer numbers, and to find the appropriate correlations for transfer coefficients.

2. FORMULATION

2.1. *Physical description*

The configuration under study is sketched in Fig. 1 where the flow over a vaporizing droplet is shown. The flow is laminar and axisymmetric with initially uniform ambient conditions specified by U'_∞, T'_∞, $\rho'_{g,\infty}$, p'_∞, and $Y_{f,\infty} = 0$.

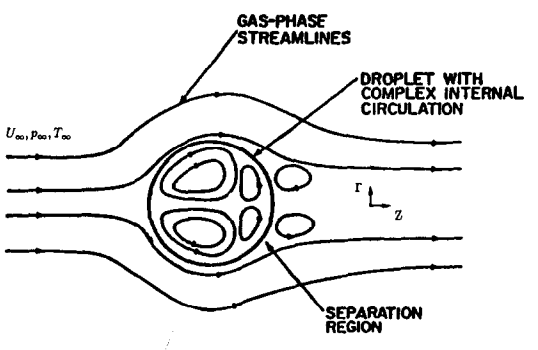

FIG. 1. Flow passing over a vaporizing droplet.

Soon after the droplet is injected into the hot gas stream, the external gas flow quickly adjusts to the presence of the droplet. A thin boundary layer is developed near the interface and a recirculation zone appears after the separation point. The shear stress at the gas/liquid interface causes the internal circulation within the droplet. A similar Hill spherical vortex is therefore formed.

As the flow develops, the drag retards the droplet (the thrust drag due to nonsymmetrical blowing, although small, has a contribution to accelerate the drop). The retardation effectively reduces the relative droplet Reynolds number which results in the decrease of surface shear.

The liquid temperature is initially uniform throughout the droplet. Part of the heat transferred from the gas phase goes into vaporization of the fuel; the remainder goes into heating of the droplet interior.

The mass transfer process is characterized by the rate of vaporization and flow convection. Fuel vapor generated at the droplet surface cannot accumulate but is convected and diffused away through the boundary layer into the gas mainstream. The molecular weight of the mixture surrounding the droplet is altered due to the presence of fuel vapor. The density and pressure distributions are also totally different from the situation of a liquid sphere without vaporization. The vaporization results in a decrease of droplet radius as well as an expansion of the wake region.

The momentum, heat, and mass transfer processes described above are coupled together and occur simultaneously. The present study employs an implicit iterative procedure to treat the coupling effect.

2.2. *Assumptions and governing equations*

The following assumptions have been made in the analysis:

(1) The Mach number is much less than unity so that the dissipation terms can be neglected.

(2) Gravity and noninertial effects are small.

(3) The droplet deformation is not important (Weber number is very small).

(4) The thermal radiant and Dufour energy flux in the energy equation, as well as the pressure and thermal diffusion flux in the species equation, are negligible.

(5) The mixture of air and fuel-vapor behaves like an ideal gas.

(6) Phase equilibrium prevails at the gas/liquid interface.

(7) The variation of thermodynamic properties of the liquid phase (except for viscosity and latent heat) is negligible.

Instead of describing the droplet motion through the gas using a Eulerian formulation, a change of reference frame from a stationary lab coordinate

frame to a system moving with the center of droplet facilitates the computation substantially. The problem can now be viewed as an impulsively started flow over a fixed droplet. Because of the change of velocity of the droplet due to the drag force, the relative velocity between the free stream and the droplet also changes at each time step. In order to return the droplet velocity back to zero, it is necessary to decelerate the gas phase flow field by applying the reversed inertia force uniformly throughout the gas phase. It is also clear that the drag coefficient will depend upon the free-stream velocity relative to the droplet; the relative velocity adjustment due to the reversed force will make the drag coefficient slightly different from its steady-state value.

The initial radius, upstream velocity and physical properties have been used to nondimensionalize the variables. The diffusion time has been selected as the time scale in this study. According to the nondimensionalization given in the Nomenclature, the nondimensional governing equations for a cylindrical coordinate system subject to the above assumptions are listed below.

Gas phase

Continuity equation

$$\frac{\partial}{\partial \tau_{Hg}}(\rho_g r)+\frac{\partial}{\partial r}(Re_g \rho_g V_r r)+\frac{\partial}{\partial z}(Re_g \rho_g V_z r)=0. \quad (1)$$

Momentum equation in r-direction

$$\frac{\partial}{\partial \tau_{Hg}}(\rho_g V_r r)+\frac{\partial}{\partial r}[Re_g r(\rho_g V_r V_r+p)]+\frac{\partial}{\partial z}(Re_g r\rho_g V_r V_z)$$
$$=\frac{2}{3}\frac{\partial}{\partial r}\left\{\mu_g r\left[2\frac{\partial V_r}{\partial r}-\frac{V_r}{r}-\frac{\partial V_z}{\partial z}\right]\right\}$$
$$+\frac{\partial}{\partial z}\left\{\mu_g r\left[\frac{\partial V_r}{\partial z}+\frac{\partial V_z}{\partial r}\right]\right\}$$
$$+Re_g p-\frac{2\mu_g}{3}\left(2\frac{V_r}{r}-\frac{\partial V_r}{\partial r}-\frac{\partial V_z}{\partial z}\right). \quad (2)$$

Momentum equation in z-direction

$$\frac{\partial}{\partial \tau_{Hg}}(\rho_g V_r r)+\frac{\partial}{\partial r}(Re_g r\rho_g V_r V_z)$$
$$+\frac{\partial}{\partial z}[Re_g r(\rho_g V_z V_z+p)]=\frac{\partial}{\partial r}\left\{\mu_g r\left[\frac{\partial V_r}{\partial z}+\frac{\partial V_z}{\partial r}\right]\right\}$$
$$+\frac{2}{3}\frac{\partial}{\partial z}\left\{\mu_g r\left[2\frac{\partial V_z}{\partial z}-\frac{V_r}{r}-\frac{\partial V_r}{\partial r}\right]\right\}. \quad (3)$$

Energy equation

$$C_{p_g}\left[\frac{\partial}{\partial \tau_{Eg}}(\rho_g r T)+\frac{\partial}{\partial r}(Pe_g r\rho_g V_r T)+\frac{\partial}{\partial z}(Pe_g r\rho_g V_z T)\right]$$
$$+r(h_{fuel}-h_{air})\left[\frac{\partial}{\partial \tau_{Eg}}(\rho_g Y_f)+\frac{\partial}{\partial r}(Pe_g \rho_g Y_f V_r)\right.$$
$$\left.+\frac{\partial}{\partial r}(Pe_g \rho_g Y_f V_z)\right]$$
$$=\frac{\partial}{\partial r}\left(r\kappa_g\frac{\partial T}{\partial r}\right)+\frac{\partial}{\partial z}\left(r\kappa_g\frac{\partial T}{\partial z}\right)$$
$$+\frac{\partial}{\partial r}\left[Le_g r(h_{fuel}-h_{air})\rho_g D_g\frac{\partial Y_f}{\partial r}\right]$$
$$+\frac{\partial}{\partial z}\left[Le_g r(h_{fuel}-h_{air})\rho_g D_g\frac{\partial Y_f}{\partial z}\right] \quad (4)$$

where $h=\int_{T_0}^{T} C_{p_g}\,dT$.

Species equation

$$\frac{\partial}{\partial \tau_S}(\rho_g r Y_i)+\frac{\partial}{\partial r}\left(\frac{Pe_g}{Le_g}r\rho_g V_r Y_i\right)+\frac{\partial}{\partial z}\left(\frac{Pe_g}{Le_g}r\rho_g V_z Y_i\right)$$
$$=\frac{\partial}{\partial r}\left(r\rho_g D_g\frac{\partial Y_i}{\partial r}\right)+\frac{\partial}{\partial z}\left(r\rho_g D_g\frac{\partial Y_i}{\partial z}\right). \quad (5)$$

Equation of state

$$p=\frac{R}{M}(\rho_g T-M). \quad (6)$$

Liquid phase

The continuity equation combined with the momentum equation can be simplified by the vorticity and stream function formulation. The stream function ψ is defined such that

$$V_r=\frac{1}{r}\frac{\partial \psi}{\partial z}$$

and

$$V_z=-\frac{1}{r}\frac{\partial \psi}{\partial r}.$$

Vorticity–stream function equations

$$\frac{\partial}{\partial \tau_{Hl}}(r\omega)+\frac{\partial}{\partial r}\left(Re_l\frac{\partial \psi}{\partial z}\omega\right)+\frac{\partial}{\partial z}\left(-Re_l\frac{\partial \psi}{\partial r}\omega\right)$$
$$=\frac{\partial}{\partial r}\left[r\frac{\partial}{\partial r}(\mu_l\omega)\right]+\frac{\partial}{\partial z}\left[r\frac{\partial}{\partial z}(\mu_l\omega)\right]-\frac{\mu_l\omega}{r}+Re_l\frac{1}{r}\frac{\partial \psi}{\partial z}\omega \quad (7)$$

$$\frac{\partial}{\partial r}\left(\frac{1}{r}\frac{\partial \psi}{\partial r}\right)+\frac{\partial}{\partial z}\left(\frac{1}{r}\frac{\partial \psi}{\partial z}\right)=\omega. \quad (8)$$

Energy equation

$$\frac{\partial}{\partial \tau_{El}}(rT)+\frac{\partial}{\partial r}\left(Pe_l\frac{\partial \psi}{\partial z}T\right)+\frac{\partial}{\partial z}\left(-Pe_l\frac{\partial \psi}{\partial r}T\right)$$
$$=\frac{\partial}{\partial r}\left(r\frac{\partial T}{\partial r}\right)+\frac{\partial}{\partial z}\left(r\frac{\partial T}{\partial z}\right). \quad (9)$$

The governing equations are transformed to generalized coordinates (ξ,η). This transformation is used to facilitate the computation with any arbitrarily mov-

ing boundary. The calculation can be easily performed on a rectangular mesh with equal spacing ($\Delta\xi = \Delta\eta = 1$). However, the above transformation requires the calculation of the Jacobian and other metrics of the transformation [17].

2.3. *Initial and boundary conditions*

2.3.1. *Initial conditions.* The gas phase initial conditions corresponding to the sudden injection of a cold droplet into a uniform flow field are:

$$V_r = p = V_f = 0, \quad V_z = T = \rho_g = 1. \tag{10}$$

Similarly, for the liquid phase, we have:

$$\psi = \omega = 0, \quad T = T_0. \tag{11}$$

At the droplet surface, we have

$$V_r = V_z = Y_f = p = 0, \quad T = T_0, \quad \text{and} \quad \rho_g = 1/T_0. \tag{12}$$

2.3.2. *Gas/liquid interface boundary conditions.* The overall behavior of droplet vaporization is very dependent on the evaluation of local properties at the interface where complex transport phenomena take place. The conditions at the interface can be derived from principles of continuity, conservation and thermodynamic equilibrium. For the convenience of calculation, the conditions are evaluated in terms of axisymmetric spherical coordinates (n, θ).

Continuity of shear stress

$$\mu_g\left(\frac{\partial V_{g,\theta}}{\partial n} - \frac{V_{g,\theta}}{a} + \frac{1}{a}\frac{\partial V_{g,n}}{\partial \theta}\right)_s = \mu_l'\left(\frac{\partial V_{l,\theta}}{\partial n} - \frac{V_{l,\theta}}{a} + \frac{1}{a}\frac{\partial V_{l,n}}{\partial \theta}\right)_s. \tag{13}$$

Continuity of tangential velocity

$$V_{g,\theta,s} = V_{l,\theta,s}. \tag{14}$$

Conservation of mass flux

$$Re_g V_{g,n} - \frac{da}{d\tau_{Hg}} = \frac{\rho_l'}{\rho_g'}\left(Re_g V_{l,n} - \frac{da}{d\tau_{Hg}}\right) \tag{15}$$

where the droplet regression rate is given by

$$\frac{da}{d\tau_{Hg}} = -\frac{1}{2}\frac{\rho_\infty'}{\rho_l'} Re_g \int_0^\pi (\rho_g V_{g,n})_s \sin\theta \, d\theta. \tag{16}$$

Continuity of temperature

$$T_{g,s} = T_{l,s}. \tag{17}$$

Conservation of energy

$$\left(\frac{\kappa_g'}{\kappa_l'}\right)\frac{\partial T_g}{\partial n}\bigg|_s = \frac{\partial T_l}{\partial n}\bigg|_s + Pe_l(\rho_g V_{g,n} L)_s\left(\frac{\rho_\infty'}{\rho_l'}\right). \tag{18}$$

Conservation of species

$$\left(D_g \frac{\partial Y_f}{\partial n}\right)_s = Re_g Sc_g [V_{g,n}(Y_f - 1)]_s. \tag{19}$$

Clausius–Clapeyron for phase equilibrium

$$p_f' = \exp(c_1 - c_2/T_{g,s}). \tag{20}$$

The mass fraction at the interface can be determined by

$$Y_f = \frac{\chi_f M_f'}{\chi_f M_f' + (1-\chi_f) M_{air}'} \tag{21}$$

where $\chi_f = p_f'/p_g'$.

Because no fluid can cross the streamlines, the liquid stream function at the interface must remain constant and must match the stream function at the axis of symmetry. Hence, $\psi = 0$ is specified at the interface. In addition, the interface boundary condition for the pressure field $(\partial p/\partial n|_s)$ is obtained from the momentum equation.

2.3.3. *Outflow* $(r = r_\infty, \pi/2 \leqslant \theta \leqslant \pi)$ *boundary conditions.*

$$\frac{D}{Dt}(V_r) = \frac{D}{Dt}(V_z) = \frac{D}{Dt}(T) = \frac{D}{Dt}(p) = \frac{D}{Dt}(Y_f) = 0. \tag{22}$$

Ryskin and Leal [18] have tested the dependence of downstream numerical oscillations on the location of the outer boundary and numerical schemes. They showed that the downstream numerical oscillation arising from the use of a centered-differencing scheme could be minimized by using a reduced grid size and employing the Neumann conditions at the outflow boundary. For this unsteady problem, the implementation of total derivative conditions at the outer boundary is most effective to minimize the numerical diffusion.

2.3.4. *Inflow* $(r = r_\infty, 0 \leqslant \theta \leqslant \pi/2)$ *boundary conditions.*

$$p = Y_f = V_r = 0, \quad T = \rho_g = V_z = 1. \tag{23}$$

2.3.5. *Axis of symmetry* $(0 \leqslant r \leqslant r_\infty, \theta = 0, \pi)$ *boundary conditions.*

Gas phase

$$V_r = \frac{\partial V_\theta}{\partial \theta} = \frac{\partial p}{\partial \theta} = \frac{\partial T}{\partial \theta} = \frac{\partial \rho_g}{\partial \theta} = \frac{\partial Y_f}{\partial \theta} = 0. \tag{24}$$

Liquid phase

$$\frac{\partial T}{\partial \theta} = \psi = \omega = 0. \tag{25}$$

2.4. *The evaluation of drag coefficients, Nusselt, and Sherwood numbers*

The global transport behavior is expressed in terms of drag coefficients, Nusselt number, and Sherwood number. The total drag consists of three components which are pressure drag, friction drag and thrust drag.

Total drag

$$C_D = C_{D,p} + C_{D,f} + C_{D,t}. \quad (26)$$

Pressure drag

$$C_{D,p} = \frac{2}{U_\infty^2} \int_0^\pi p_s \sin 2\theta \, d\theta. \quad (27)$$

Friction drag consists of contributions from viscous normal and tangential shear stress:

$$C_{D,f} = \frac{4}{Re_g U_\infty^2} \int_0^\pi \mu_g \left[\left(\frac{\partial V_{g,\theta}}{\partial n} - \frac{V_{g,\theta}}{a} + \frac{1}{a} \frac{\partial V_{g,n}}{\partial \theta} \right)_s \sin^2 \theta - \frac{1}{3} \left(2 \frac{\partial V_{g,n}}{\partial n} - \frac{2V_{g,n}}{a} - \frac{1}{a} \frac{\partial V_{g,\theta}}{\partial \theta} - \frac{V_{g,\theta}}{a} \frac{\cos\theta}{\sin\theta} \right)_s \sin 2\theta \right] d\theta. \quad (28)$$

Thrust drag due to the reaction of momentum flux at the interface is given by

$$C_{D,t} = \frac{2}{U_\infty^2} \int_0^\pi [\rho_g V_{g,n} (V_{g,n} \sin 2\theta - 2V_{g,\theta} \sin^2 \theta)]_s \, d\theta. \quad (29)$$

The droplet deceleration is determined from the total drag force

$$\frac{dU_d}{d\tau_{Hg}} = -\frac{3}{8} \frac{\rho'_\infty}{\rho'_l} \left(\frac{U_\infty^2}{a} \right) Re_g C_D. \quad (30)$$

The definitions of average Nusselt and Sherwood numbers are given by

$$Nu_{av} = \frac{a \int_0^\pi \kappa_g \frac{\partial T_g}{\partial n} \sin\theta \, d\theta}{1 - T_{av,s}} \quad (31)$$

$$Sh_{av} = \frac{a \int_0^\pi \rho_g D_g \frac{\partial Y_f}{\partial n} \sin\theta \, d\theta}{Y_{f_{av,\infty}} - Y_{f_{av,s}}}. \quad (32)$$

The values and formulas for the thermophysical properties for both gas and liquid phases of different hydrocarbon fuels can be found in Vargaftik [19] and Abramzon and Sirignano [20]. Wilke's formula is employed to calculate mixture viscosity and thermal conductivity.

3. SOLUTION PROCEDURE

The nonlinear and highly coupled equations make the analytical solution very difficult. In the present study, the system of equations is discretized by implicit finite-difference schemes. For the spatial derivatives, the second-order-accurate centered-difference scheme is employed. The time derivative is represented by a first-order approximation.

The direct solution of the system requires inversions of massive matrices which are not allowed on the workstation currently employed. The procedure adopted in the present study solves the equations sequentially. The whole set of equations is iterated until the convergence criteria for stream function, mass conservation and pressure correction are satisfied. Hence the whole procedure is implicit intrinsically. A modified ICE method, originally developed by Westbrook [21], is used to update the most recent values of velocity, pressure and density during the iterative procedure. The mass conservation equation is indirectly satisfied by the pressure correction equation. The stream function and pressure correction equations are of the elliptic type and can be efficiently solved by the successive-over-relaxation (S.O.R.) method. The momentum, temperature and species equations of the gas phase as well as the vorticity and temperature equations of the liquid phase are parabolic in nature and are solved by an alternate direction predictor–corrector (ADPC) method which provides the unconditional stability with little computational penalty for implicit methods [22]. In order to reduce the coupling effects, the nonlinear interface boundary equations are treated by a quasi-linearization technique and solved directly by the inversion of a tridiagonal block matrix.

Since the reference frame is fixed to the droplet, a reversed D'Alembert force due to the drag force on the droplet must be applied to the gas phase flow field. The change of relative velocity between the free stream and the droplet is determined by

$$\Delta U_{rc} = \Delta \tau_{Hg} \frac{dU_d}{d\tau_{Hg}}. \quad (33)$$

The gas flow velocity throughout the field is therefore numerically adjusted to represent properly the reversed inertia force by

$$U(r, z, \tau + \Delta\tau) = U^*(r, z, \tau) + \Delta U_{rc}. \quad (34)$$

The physical grid system features variable spacing in the radial direction and uniform spacing in the angular direction. A fine spacing is required for accuracy near the droplet interface at both gas and liquid sides, where the gradients are expected to be large. On the contrary, a coarse spacing is employed in the far stream. In order to keep a dense grid distribution at the droplet interface, the grid locations have to be adjusted at each time step to accommodate droplet surface regression. In the present study, the outer boundary remains fixed in position; therefore, the grid adaptation requires a stretch of grid size outside the droplet and a shrinking of grid size within the droplet. It is noted that the metrics of transformation have to be updated whenever the grid system moves.

The overall procedure iterates the sequential solutions of governing equations and boundary conditions with grid and relative velocity adjustment until the convergence is achieved. The number of iterations

required for convergence in the pressure correction equation as well as within the overall iteration loop is dependent upon the physical parameters used in each case. For decreased vaporization rates, the requisite number is very much reduced. After convergence is reached, the drag coefficients and average Nusselt and Sherwood numbers are evaluated at prescribed time intervals.

Since the pressure correction equation is elliptic in nature, the location of the outer boundary of the computational domain may affect the numerical solution. Sundararajan and Ayyaswamy [15] suggested that r_∞ must be at least ten times the droplet radius. In the present analysis the mesh in the gas phase consists of 35×31 nodes with $\Delta\theta = 6^\circ$ and $\Delta r = 0.02$ adjacent to the droplet surface and expanding at a rate of 14.5% to $r_\infty = 16.6$, which is believed to be large enough to include the region of influence from the recirculatory wake and to ensure that the boundary conditions at the far-stream are truly realized. The liquid side has 30×31 nodes with $\Delta r = 0.02$ at the droplet interface enlarging at a rate of 5.5% towards the origin. The computational mesh makes use of equal spacings ($\Delta\eta = \Delta\xi = 1$) in both rectangular coordinates which are fixed with time.

Two numerical experiments regarding the sensitivity of results by changing grid size and time-step size have been conducted. The preliminary results indicate that the further refinement of grid size or enlargement of r_∞ only makes a change less than 0.1% in the drag coefficient. All the results are relatively insensitive to the time-step size.

Each equation is individually solved by a modular routine which can be easily implemented and tested on the Apollo domain-3000 workstation. The final computations are performed on a CRAY X-MP supercomputer. A time-step size of 0.001 is chosen initially. Once the solution approaches convergent stage, an increase of time-step size while maintaining accuracy is possible. For a typical run, the average CPU time per time-step is about 0.8 s.

4. RESULTS AND DISCUSSION

It is always a good practice to verify and benchmark against the results of similar problems before extensive numerical calculations are made. Since there exists no known exact solution for the problem under consideration, a check for the code is performed by comparing the results of the solid sphere case and the liquid sphere case (without vaporization and gas phase mass transfer) with the steady-state numerical correlations presented in ref. [1]. The predicted drag coefficient for the solid sphere case is within 2% of the standard drag coefficient which can be expressed as

$$C_D = \frac{24}{Re_g}(1 + 0.1935 Re_g^{0.6305}); \qquad 20 \leqslant Re_g \leqslant 260. \tag{35}$$

The Nusselt and Sherwood numbers agree within 3 and 5% respectively with the correlations presented in Table 5.4 of ref. [1]. For the case of a liquid sphere, the component drag and total drag values are predicted within 7% of the values given in Table 5.6 of ref. [1]. The small discrepancy is attributed to the constant property assumption used in ref. [1]. A test run of the present problem with the same parameters used in ref. [16] was also conducted. The calculation has only been performed up to 1250 residence time due to economical constraints. The total drag coefficient agrees within 10% of their numerical correlation. With the above verification, it is safe to confirm the reliability of the code.

The base case study is selected as a cold n-octane fuel droplet suddenly injected into the hot gas stream. The values of physical parameters in the base case are given in Table 1. An extensive parameter study by changing initial droplet temperature, ambient temperature, initial Reynolds number, fuel types, and droplet heating model has been conducted. Table 2 summarizes the main parameters used for different cases examined in the present research.

The results are presented in the following four subsections. The first three subsections give a description of global flow field and the local, as well as overall, behavior of the single droplet for the baseline case. The variation of drag coefficient due to different parameters is given in the fourth subsection. The subsequent subsection presents the possible correlations for the drag coefficient and Nusselt and Sherwood numbers. The time scale used for the following discussion is the gas phase hydrodynamic diffusion time.

4.1. *Results for the global flow field*

Typical contour plots of mass fraction, temperature, and vorticity, as well as liquid phase streamlines and gas phase velocities, are presented in Figs. 2(a)–(f). The convective effect is apparent by the fore–aft

Table 1. Values of physical parameters used in the isolated droplet base case computation

Parameter	Value
Initial Reynolds number, gas phase $Re_g = 2a'_0 U'_{\infty,0} \rho'_{g,\infty}/\mu'_{g,\infty}$	100.0
Relative velocity of droplet [m s^{-1}]	25.0
Free stream temperature [K]	1250.0
Combustor pressure [atm]	10.0
Prandtl number, gas phase	0.74
Prandtl number, liquid phase	8.59
Schmidt number, gas phase	2.36
Molecular weight, oxidizer [kg kmol^{-1}]	29.0
Molecular weight, fuel, n-octane [kg kmol^{-1}]	114.2
Droplet initial temperature [K]	300.0
Viscosity ratio, $\mu'_l/\mu'_{g,\infty}$	10.49
Density ratio, $\rho'_l/\rho'_{g,\infty}$	251.93
Specific heat at constant pressure ratio, $C'_{p_{l,0}}/C'_{p_{g,\infty}}$	1.87
Latent heat/specific heat of liquid [K]	135.95

Table 2. Main parameters considered in each case of the isolated-droplet study

Case†	T_∞ [K]	Re_g	Fuel	Physical property
1	1250	100	n-octane	variable
2	1800	100	n-octane	variable
3	800	100	n-octane	variable
4	1800	100	n-octane	constant ($T_{ref} = T_\infty$)
5	1800	100	n-octane	constant ($T_{ref} = (T_\infty + T_{L0})/2$)
6	800	100	n-octane	constant ($T_{ref} = T_\infty$)
7	800	100	n-octane	constant ($T_{ref} = (T_\infty + T_{L0})/2$)
8‡	1250	100	n-octane	variable
9	1250	150	n-octane	variable
10	1250	50	n-octane	variable
11§	1250	100	n-octane	variable
12	1250	100	n-decane	variable
13	1250	100	n-hexane	variable

† Initial droplet temperature = 300 K, axisymmetric calculation for all cases except Cases 8 and 11.
‡ Infinity conductivity model for the liquid phase.
§ Initial droplet temperature = 400 K.

asymmetry in each plot. The boundary layers surrounding the droplet can be easily observed from the gas phase velocity distribution as shown in Figs. 2(a) and (b) for two different times. At early times, there is no indication of flow separation because the separation is suppressed by the surface movement (which will be explained later). Later, the boundary layers only cover 138° in azimuthal position, and a near wake region appears behind the droplet. The magnitude of velocity, as displayed in Fig. 2(b), has been reduced, owing to the retardation by the drag force. The temperature and mass fraction contours, as portrayed in Figs. 2(c) and (d), respectively, do show the presence of the boundary layer and wake. The diffusing fuel-vapor is convected downstream, forming a concentration wake at the rear.

The liquid phase streamlines in Fig. 2(e) show a single large vortex, roughly resembling Hill's spherical vortex, in the interior of the droplet. The circulation decreases with time. The vorticity contours presented in Fig. 2(f) are concentrated at the front portion of the droplet and are then convected downstream. Later, the vorticity diffuses outward and the intensity is weakened, mainly due to the reduction in Reynolds number. A local peak on the aft side, which represents a recirculating eddy attached at the surface, is observed. When flow separation occurs, the distribution becomes highly asymmetric. The surface blowing inhibits the appearance of a small secondary internal vortex of opposite direction which might occur near the rear stagnation point.

The detailed droplet heating history may be seen from Figs. 3(a) to (c). During the very early time ($\leqslant 1$), a large temperature gradient exists near the surface and the motion of the liquid phase is negligible. The energy transfer mode within the droplet is dominated by conduction. As the internal circulation increases, convection gradually tends to dominate. The isotherms at time = 5 show the large temperature variation from the surface to the vortex center. The similarity between the isotherms and streamlines in the liquid phase indicates the influence of internal circulation. The assumption of high Peclet number used in a vortex model [5–7] is reliable at this stage. As the gas phase shear stresses decrease, the circulation lessens gradually such that convection becomes less important and the relative effect of conduction grows again. This type of behavior is more evident for the lower transfer number case where the Peclet number is smaller.

4.2. *Local properties along the droplet surface*

Since the overall drag coefficient, Nusselt and Sherwood numbers of the droplet are very sensitive to the transport processes occurring at the gas/liquid interface, it is necessary to have a detailed understanding of some important properties at the droplet surface. The instantaneous droplet Reynolds number, the separation point (S.P.), the zero stress point, and the position for the local maximum (or minimum) predicted in the numerical calculation, as well as the separation point on the liquid sphere in the absence of vaporization, are indicated at different times in Figs. 4(a)–(g).

The surface-shear stress distribution at different times shown in Fig. 4(a) indicates that the shear stress decreases with time. This can be realized by the following facts: (1) with the onset of surface motion, the velocity gradient at the droplet surface decreases; (2) the surface blowing effect, which increases the thickness of the boundary layer and reduces the velocity gradient, grows as vaporization becomes stronger; and (3) as droplet heating continues, the mass fraction at the surface also keeps increasing, thus yielding lower values of viscosity of the mixture.

The decrease of strength of the negative shear stress is due to the decrease of volume and strength of the wake recirculation which is mainly caused by the reduction of the Reynolds number.

The time variation of the surface tangential velocity

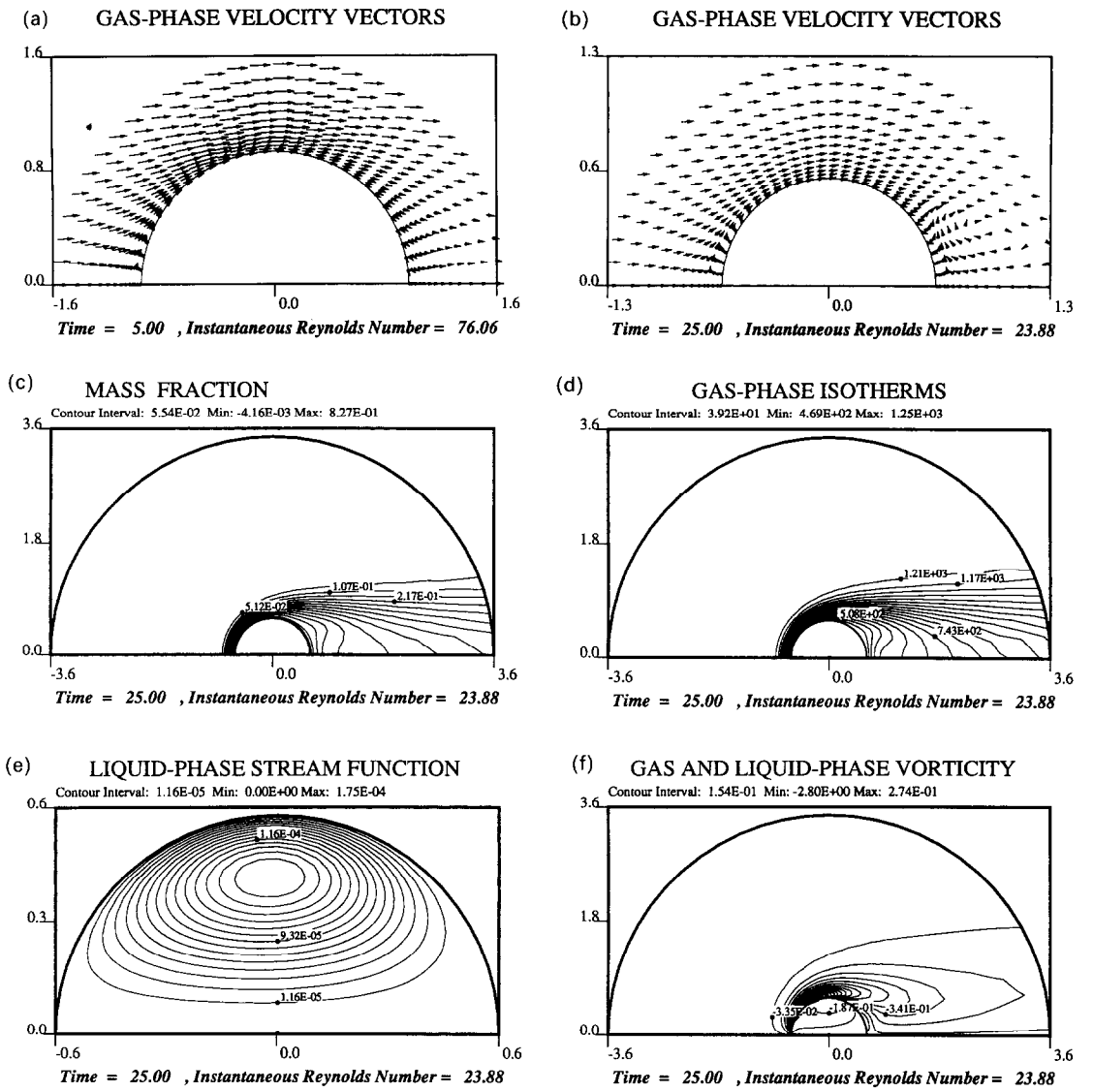

FIG. 2. (a) Instantaneous velocity of gas phase at time = 5. (b) Instantaneous velocity of gas phase at time = 25. (c) Mass fraction contour plot at time = 25. (d) Gas phase temperature contour plot at time = 25. (e) Stream function of liquid phase at time = 25. (f) Vorticity contour plot of gas and liquid phases at time = 25.

distribution shown in Fig. 4(b) seems to vary with $\sin\theta$, which is in qualitative agreement with the classical vortex solution. The surface tangential velocity, originally zero, is brought to a maximum by the shear stresses and then decreases as the shear stresses diminish. Note that the angular location of the maximum velocity remains unchanged except during the final period when the location of the maximum shifts forward of the $\theta = 90^\circ$ plane.

The distribution of vorticity along the droplet surface during transient development, as shown in Fig. 4(c), is very similar to that of the shear stress. The surface vorticity is obtained from

$$\omega_l = \frac{\mu_g'}{\mu_l'}\left[\frac{\partial V_{g,\theta}}{\partial n} - \frac{V_{g,\theta}}{a} + \frac{1}{a}\frac{\partial V_{g,n}}{\partial \theta}\right]_s - 2\left.\frac{\partial V_{l,\theta}}{\partial n}\right|_s. \quad (36)$$

The dominant term is $(\partial/\partial n)V_{g,\theta}$, which is also the main term contributing to the shear stress. It is clear that $\omega \sim 1/\delta \sim Re_g^{1/2}$. Hence, it is expected that the effects of internal circulation, boundary layer blowing, and reduction of gas phase Reynolds number will cause the surface vorticity to diminish. If the flow separation point is defined as the point where vorticity changes sign, the results indicate that separation occurs at a very early time. When the surface starts moving, the separation is suppressed. At later times, the surface velocity is reduced and the normal surface blowing velocity increases. As a result, the separation point moves in the upstream direction. This behavior is different from that of the low transfer number case where the surface velocity is usually small and the surface motion can only delay the onset of flow sep-

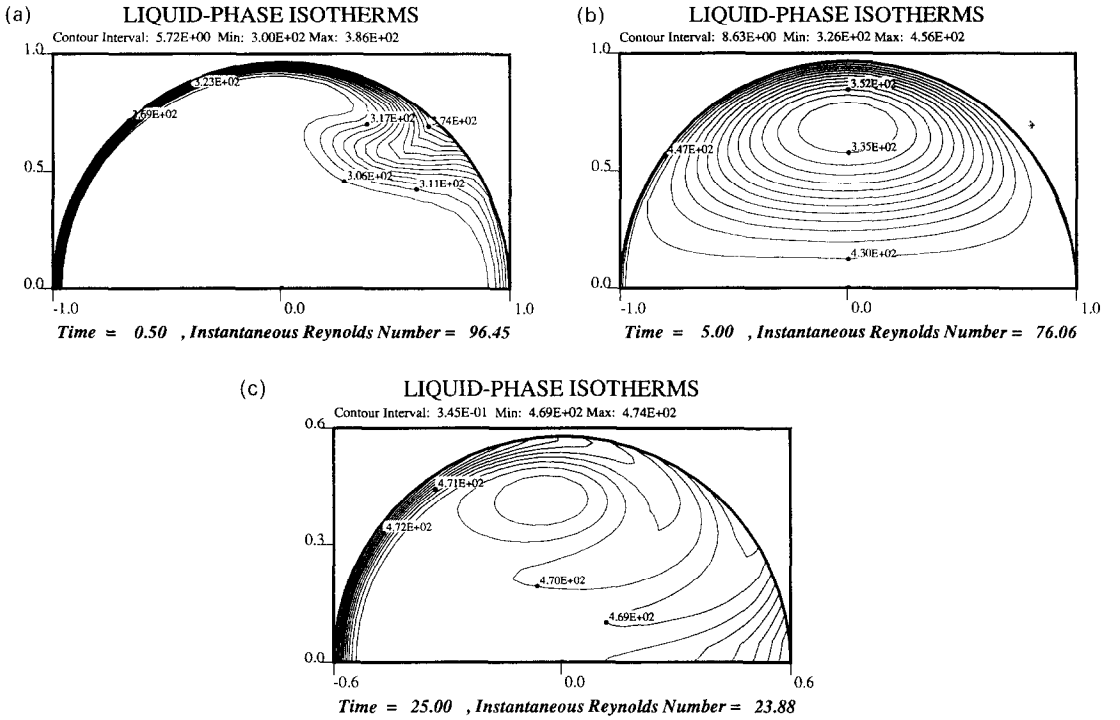

FIG. 3. Transient history of droplet heating. Time = 0.5 (a), 5 (b) and 25 (c).

aration. The flow separation is observed throughout most of the droplet lifetime. The theoretical separation point for the nonvaporizing liquid sphere moves rearward as the Reynolds number decreases with time [1]. The prediction of the separation point for a vaporizing droplet is hence totally different from that for a nonvaporizing liquid sphere.

Figure 4(d) shows the pressure distribution on the droplet surface. The recirculation wake dissipates part of the kinetic energy. As a result, the pressure cannot recover to the stagnation value. The pressure profile is essentially determined from the balance between the diffusive and convective transport of vorticity. Vaporization enhances the outward convection of vorticity and thus causes more pressure loss. However, the additional kinetic energy resulting from surface blowing is absorbed by the recirculation wake. This can result in some pressure recovery.

The angular variation of local Nusselt number at different times is shown in Fig. 4(e). The Sherwood number behaves similarly. The temperature (or mass fraction) gradient at the surface and thus Nu_{local} (or Sh_{local}) are greatest at the front stagnation point and decrease with polar angle; see also Figs. 2(c) and (d). The minimum does not necessarily occur aft of the separation point, as for the case of low transfer number. The increase at the rear of the droplet is caused by the action of the recirculating wake. The reduction in the Nusselt and Sherwood numbers with time is mostly attributed to the decay in Reynolds number.

Figure 4(f) shows the time variation of the surface temperature distribution. The surface temperature is nonuniform during most of the droplet lifetime. The rise of temperature at the rear portion is predominantly caused by the hot far-stream returned by the recirculating wake. After droplet heating begins to diminish, the surface temperature shows some degree of uniformity. However, the constant surface temperature assumption is improper when the droplet heating persists.

The transient development of the surface normal velocity is shown in Fig. 4(g). The gas surface normal velocity is primarily determined by the rate of evaporation. Hence, the normal velocity increases when the surface temperature increases with time. As the surface temperature approaches the wet-bulb temperature, the fuel-vapor mass-fraction at the surface remains constant and the boundary layer thickness keeps growing. As a result, the normal velocity decreases. The maximum normal surface velocity occurs at the front stagnation point, while the minimum is located near the separation point.

4.3. *Overall transfer coefficients*

Obviously, droplet vaporization is an inherently transient process. A summary of transient droplet life history is presented in Fig. 5. The droplet heating is indicated by the ratio of Q_l, the energy spent for droplet heating, to Q_g, the total heat flux obtained from the gas phase. The results indicate that both transient droplet heating and reduction in Reynolds number persist during most of the droplet lifetime. These two transient effects constitute the major sources of the unsteady behavior of this problem. The average volumetric temperature, which is nondimensionalized in the figure as $(T_v - T_0)/(T_{\text{wet}} - T_0)$, is lower than the

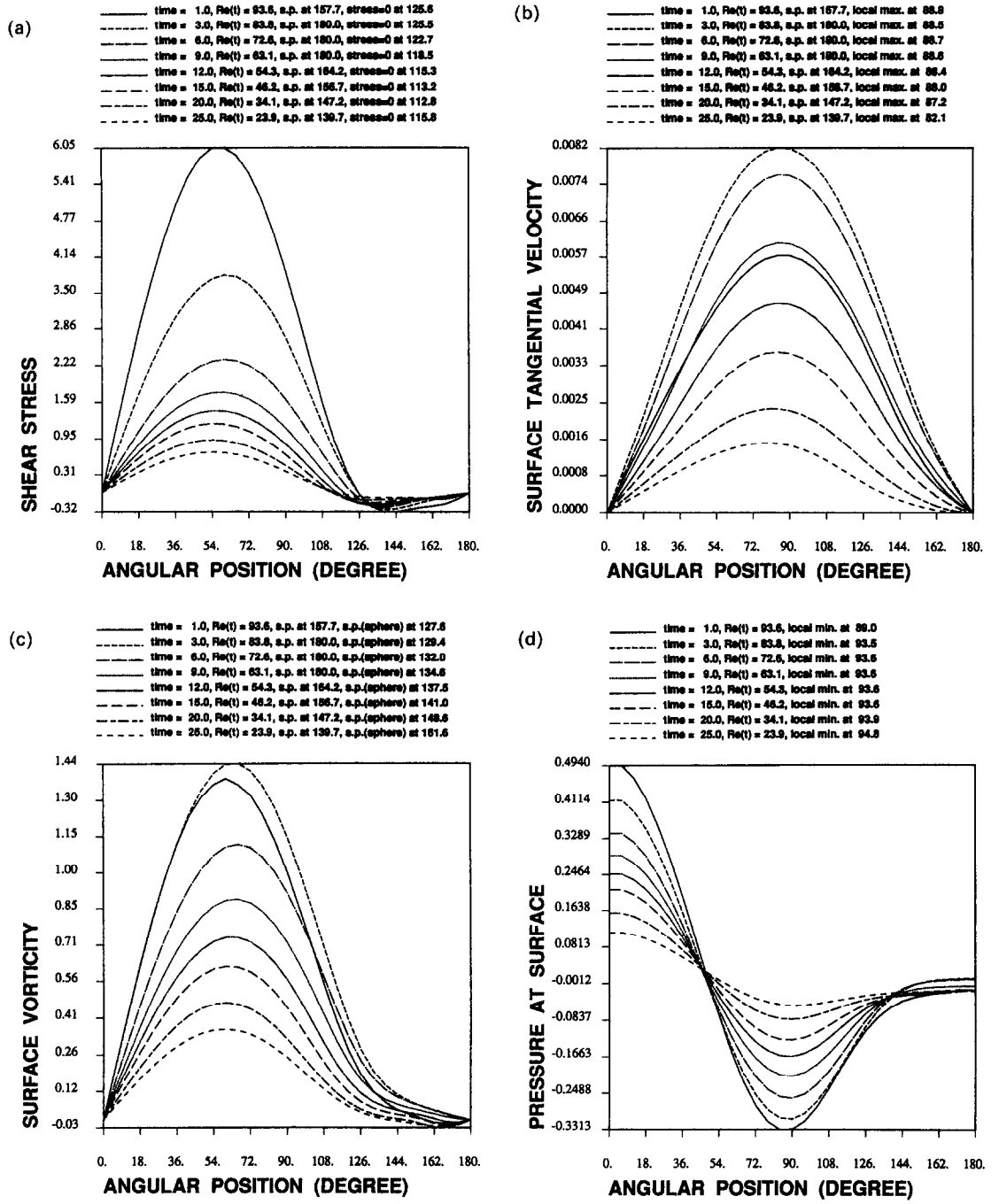

FIG. 4. (a) Surface shear stress distribution at different times. (b) Surface tangential velocity distribution at different times. (c) Surface vorticity distribution at different times. (d) Surface nondimensional pressure distribution at different times.

average surface temperature $(T_s - T_0)/(T_{wet} - T_0)$, until the droplet has reached practically wet-bulb temperature when more than half of the mass is vaporized.

We now switch our attention to the overall characteristics of momentum, heat, and mass transfer to the droplet. Figure 6 shows the variation of drag coefficients of droplets initially at three different ambient temperatures (Cases 1, 2, and 3) as a function of hydrodynamic diffusion time. Also shown in this figure is the H–N–R (Haywood, Nafziger and Renksizbulut [16]) drag correlation which is based on the numerical results of an isolated moving drop vaporizing in its own fuel vapor. The H–N–R correlation is given by

$$C_D(1+B_{H,film})^{0.2} = \frac{24}{Re_m}(1+0.2Re_m^{0.63}); \quad 10 \leqslant Re_m \leqslant 300 \tag{37}$$

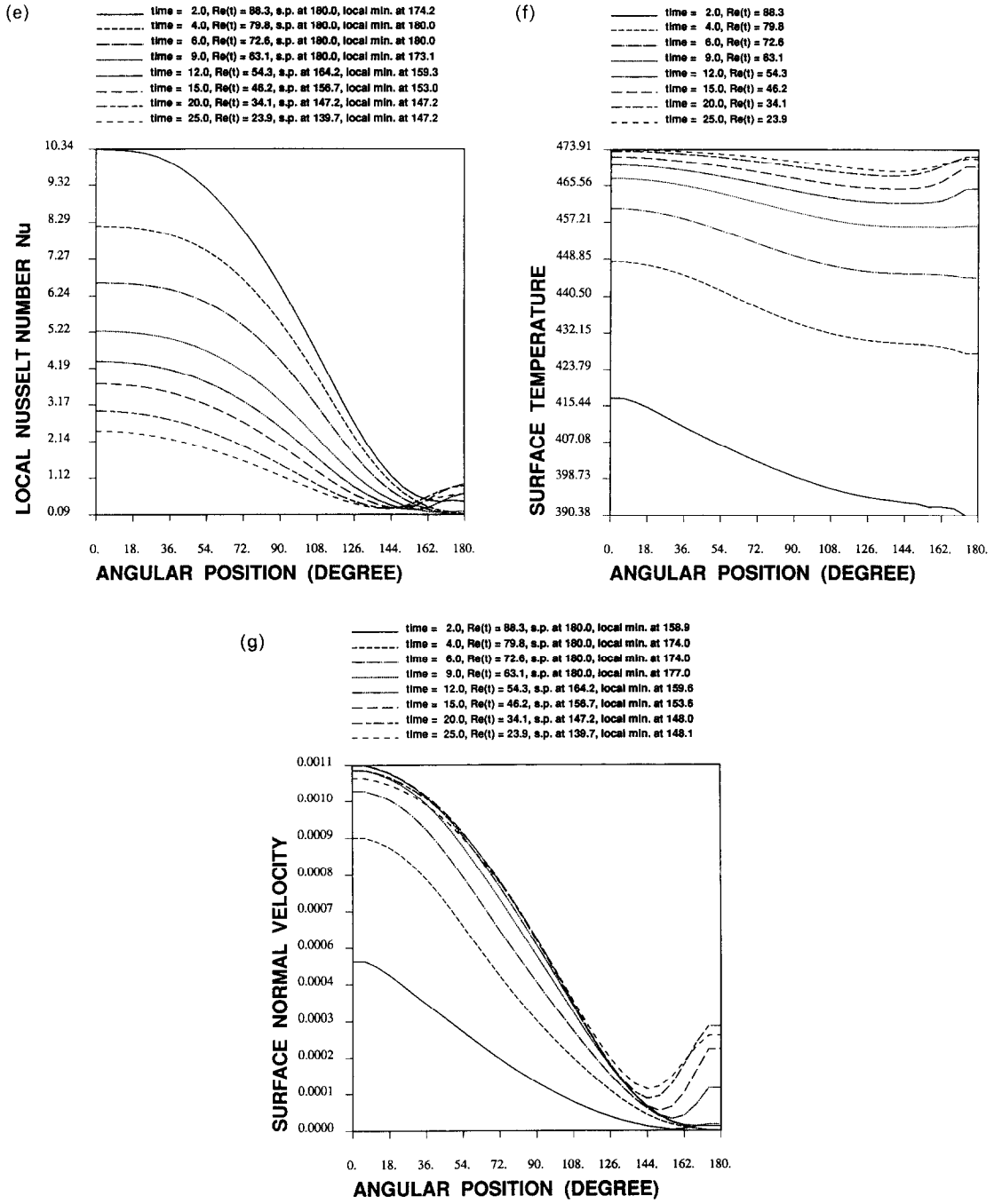

FIG. 4. (e) Local Nusselt number distribution at different times. (f) Surface temperature distribution at different times. (g) Surface normal velocity distribution at different times.

where $B_{h,film}$ is defined to account for droplet heating. The gas film condition is the average of ambient and droplet surface conditions:

$$B_{H,film} = \frac{Cp'_{g,film}(T'_\infty - T'_s)}{L'_s}\left(1 - \frac{Q'_l}{Q'_g}\right). \quad (38)$$

Due to the sudden injection of the drop into a uniform flow-field, the time required for the flow-field to relax from the initially impulsive motion can be estimated as $\Delta t_{relax} \sim 2R_\infty/U_\infty \sim 0.4$ diffusion times. During the initial relaxation period, the drag coefficient falls rapidly. Subsequently C_d increases as a result of a reduction in the Reynolds number. However, for the higher ambient temperature case where the large heat flux makes droplet vaporization rate grow rapidly during the early portion of its lifetime, the drag coefficient is therefore significantly decreased due to boundary layer blowing. For all cases, C_d tends to increase with time during the final portion of the calculation, which implies that the

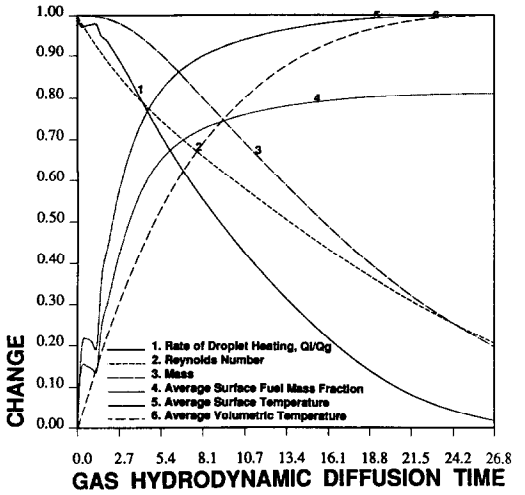

FIG. 5. The transient evolution of the rate of droplet heating, Reynolds number, mass, average surface fuel mass fraction and temperature, and average volumetric temperature.

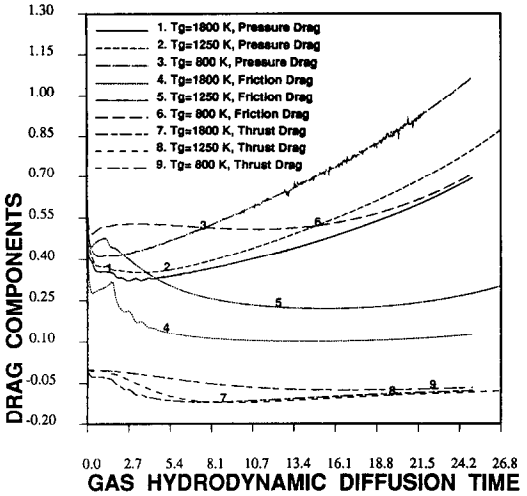

FIG. 7. Time variation of three drag components for different ambient temperatures.

reduction in Reynolds number takes control in determining drag coefficients. The H–N–R drag correlation does not apply well in our cases. The deviation can be as much as 20% of total drag.

Three components of drag coefficients are shown in Fig. 7. It is clear that the major difference in total drag coefficients for the three different ambient temperature cases reported comes primarily from the values of the friction drag components. Higher surface blowing can reduce the friction drag by a large amount. The pressure drag coefficient increases steadily as a result of the reductions in upstream velocity. It is noteworthy that the thrust drag is no longer negligible for the high transfer number case. The contribution from the $-V_{g,n}V_{g,\theta}\sin^2\theta$ term may account for about a 10% reduction of the total drag. This term physically represents the thrust force as the reaction of tangential momentum being convected radially outwards and serves to accelerate the droplet. The recoil force due to the impact of the outward flux, $V_{g,n}V_{g,n}\sin 2\theta$, is negligible.

Figure 8 shows the average Nusselt numbers of these three cases and their corresponding H–N–R Nusselt number correlations which can be expressed as

$$Nu_{\text{film}}(1+B_{\text{H,film}})^{0.7} = 2+0.57Re_{\text{m}}^{1/2}\,Pr_{\text{film}}^{1/3}. \quad (39)$$

The Nusselt number falls during the initial relaxation period. Further reduction in Nusselt number is attributed mainly to a Reynolds number reduction and an increase of boundary layer thickness due to surface blowing. Increases in the ambient temperature produce decreases in the Nusselt number. Again, our numerical results do not agree with the H–N–R cor-

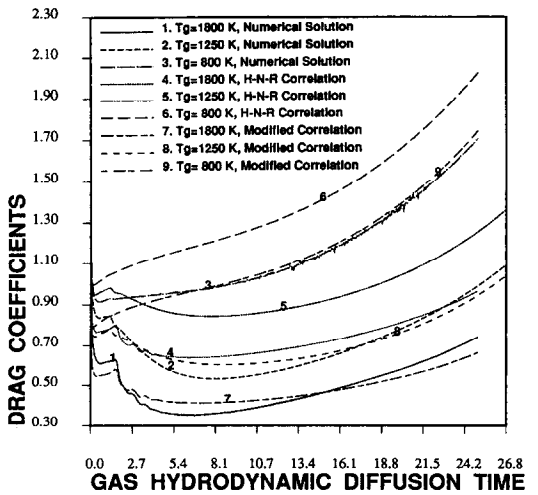

FIG. 6. Time variation of drag coefficients for different ambient temperatures as well as comparison with H–N–R correlation and modified correlation.

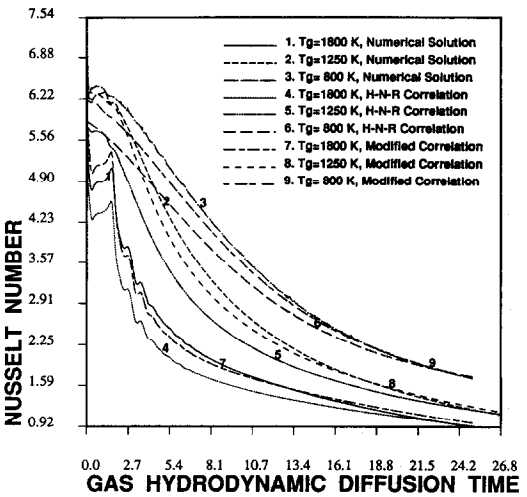

FIG. 8. Time variation of average Nusselt numbers for different ambient temperatures as well as comparison with H–N–R correlation and modified correlation.

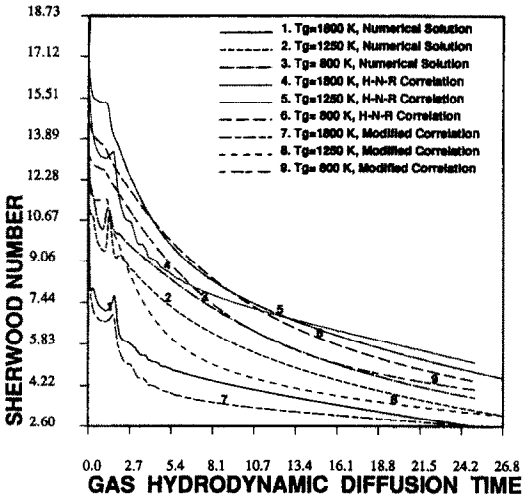

FIG. 9. Time variation of average Sherwood numbers for different ambient temperatures as well as comparison with H–N–R correlation and modified correlation.

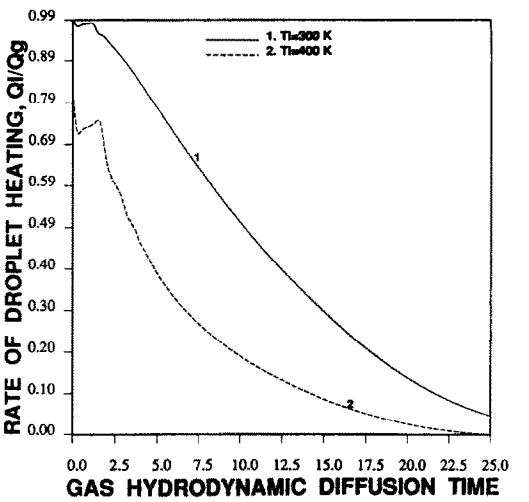

FIG. 11. Time variation of the rate of droplet heating for initial droplet temperatures.

relation. However, the discrepancy becomes smaller during the final part of the calculation when the surface temperature approaches the wet-bulb temperature.

The Sherwood number, which represents the transient dynamics of the mass transfer, is shown in Fig. 9. The general trend of variation is very similar to that of Nusselt number. Our numerical value is lower than the value predicted by the correlation of H–N–R, which is given by

$$Sh_{\text{film}}(1+B_{\text{M,film}})^{0.7} = 2+0.87Re_{\text{m}}^{1/2}Sc_{\text{film}}^{1/3} \quad (40)$$

where

$$B_{\text{M,film}} = \frac{Y_{\text{f,s}} - Y_{\text{f},\infty}}{1 - Y_{\text{f,s}}}.$$

4.4. *The parameter study*

Results for different initial droplet temperatures (300 K vs 400 K as in Cases 1 and 11, respectively) are shown in Fig. 10. It is very clear that for the higher initial droplet temperature case, the surface blowing effect is more significant than that of the lower droplet temperature case during a large portion of the droplet lifetime. Hence, the former experiences lower drag than the latter. Figure 11 shows the portion of total heat flux that goes into heating of the drop interior. The droplet with higher initial temperature would expend most of the available heat energy on the evaporation process. On the contrary, the droplet with lower initial temperature has to expend most of the available energy to heat itself first, with the remaining energy used for vaporization. The heating process for the low initial droplet temperature case is slower and will persist longer than for the high initial droplet temperature case. As the surface temperatures of both cases approach asymptotically the same wet-bulb temperature (i.e. same transfer number), the drag coefficient is essentially controlled by the Reynolds number. Also shown in Fig. 10 is the solid sphere correlation which can be grossly inaccurate due to the high mass transfer at the surface. Since the surface blowing effect is much stronger for the high initial droplet temperature case, the Nusselt and Sherwood numbers are smaller than those for the low droplet temperature case.

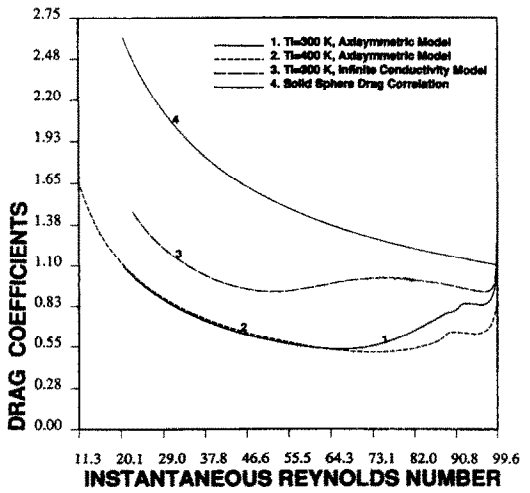

FIG. 10. Time variation of drag coefficients for the cases of different initial droplet temperatures and different droplet heating models.

Figure 10 shows a comparison of results from an infinite conductivity liquid phase model, where the liquid phase temperature is assumed to be uniform in space but varying with time (Cases 1 and 8). The no-slip boundary condition is also applied at the droplet surface. The results indicate that the infinite conductivity case predicts higher drag during most of the droplet lifetime. For the infinite conductivity model, heat flux is distributed uniformly over the liquid droplet interior. Thus, the surface temperature initially rises slowly resulting in a very weak vaporization rate, as well as in a high drag coefficient. The transient heating period is relatively short. Because of the larger driving temperature potential, the droplet eventually

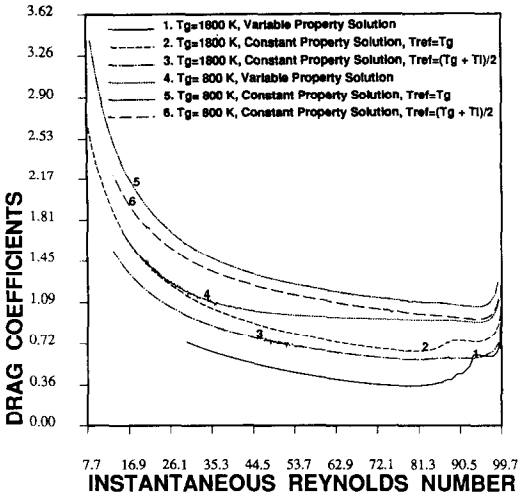

FIG. 12. Comparison of drag coefficients for constant property calculations with different reference temperatures and variable property calculations at different ambient temperatures.

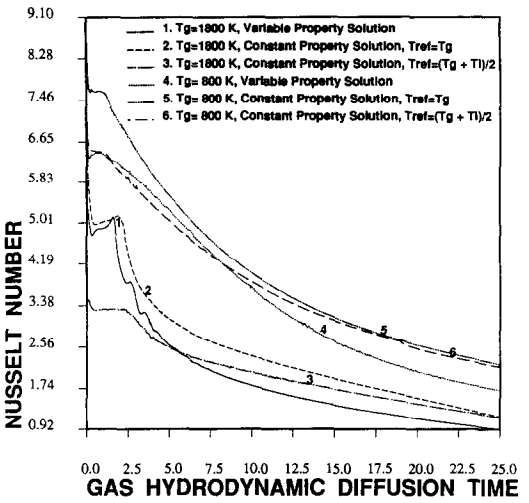

FIG. 13. Comparison of Nusselt numbers for constant property calculations with different reference temperatures and variable property calculations at different ambient temperatures.

receives more heat flux than that calculated from our model. As a result, the surface temperature does eventually increase very significantly, and the vaporization rate grows quickly while the drag coefficient is reduced significantly. The drag coefficient during the later period is primarily determined by the reduction of the Reynolds number, as already illustrated in previous cases.

The effect of variable thermophysical properties is very important for the large range of temperatures considered in the present study. Four calculations with two different ambient temperatures have been conducted by assuming constant properties (except for gas phase density) that are evaluated at the reference temperature. The reference temperatures are selected to be the ambient temperature for cases 4 and 6 and average of the ambient and surface temperatures for cases 5 and 7. Since the global behavior is evaluated at the interface, where the gas phase composition is very different from the pure gas at the free stream, the constant property calculations are expected to predict totally different transfer coefficients. The results in Fig. 12 show that the constant property case can overestimate the drag coefficient by 20% or more compared to the variable property case. The discrepancy increases as the evaporation rate becomes significant (when the droplet reaches the wet-bulb temperature). The discrepancy is attributed to the change in thermo-physical properties at the interface and the change in the flow field caused by the property gradients. A similar trend for Nusselt number is observed in Fig. 13. However, the Sherwood numbers from the constant property calculations with average reference temperature give better agreement with those from variable property calculations as presented in Fig. 14.

Calculations for three different initial Reynolds numbers (Cases 1, 9, and 10) are presented in Fig. 15. It is observed that a lower initial Reynolds number results in a higher drag coefficient at early times due to the smaller convective momentum transport, which usually causes lower pressure recovery at the rear of the droplet. It is also noteworthy that the three drag coefficients again asymptotically approach a certain form which is governed by the Reynolds number only. This is because the same effective transfer number has been reached for all three cases.

The final parameter study is concerned with the fuel volatility (Cases 1, 12, and 13). The more volatile fuel uses a large fraction of the energy flux to provide the latent heat for vaporization and vaporizes faster than the heavier fuels. The less volatile fuel expends most

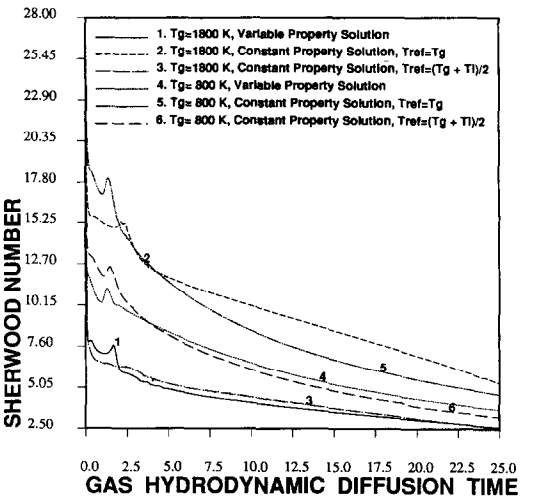

FIG. 14. Comparison of Sherwood numbers for constant property calculations with different reference temperatures and variable property calculations at different ambient temperatures.

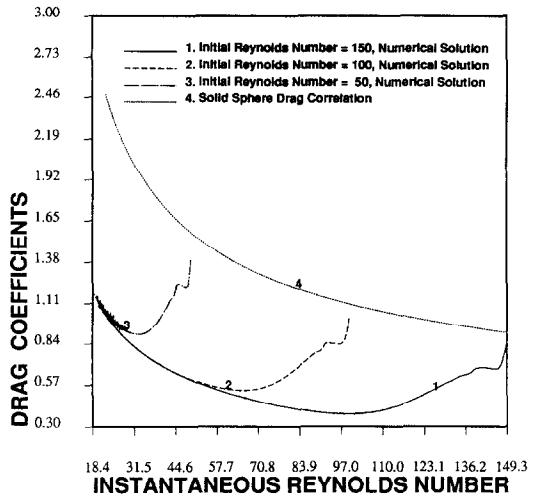

FIG. 15. Time variation of drag coefficients for different initial Reynolds numbers.

of the available energy in heating the droplet. As a result, the surface temperature rises very slowly and the effect of surface blowing is less noticeable. The reduction of drag due to surface blowing is more pronounced for volatile fuels, as indicated in Fig. 16.

4.5. *Correlations for the drag coefficient and Nusselt and Sherwood numbers*

With the results of the above cases, which cover a wide range of transfer numbers as well as Reynolds and liquid Peclet numbers, it is desirable to obtain the correlations of drag coefficient and Nusselt and Sherwood numbers as functions of the important parameters. Since these transport quantities are determined by the combined influence of surface blowing and vaporization, the internal circulation, and the unsteady effects related to droplet deceleration, a complete correlation which covers a wide range of all parameters is not easy to obtain.

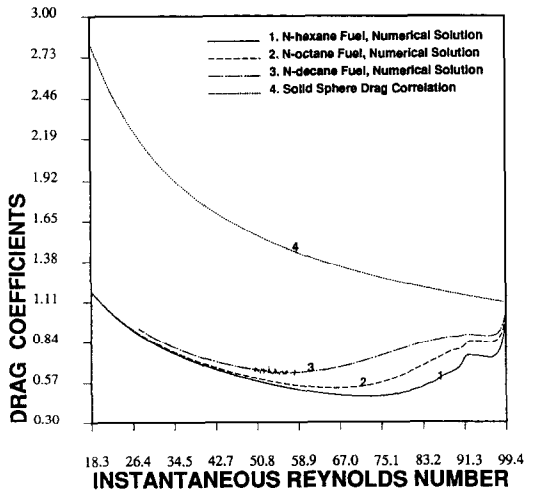

FIG. 16. Time variation of drag coefficients for different fuels.

We have employed a nonlinear regression method using least squares to fit more than 2700 data points and yielded the following modified correlations for drag coefficient and Nusselt and Sherwood numbers. The new correlations show a good agreement (all within 10%) with our numerical results, as shown in Figs. 6, 8 and 9. These corrections are expressed by

$$C_D(1+B_{H,film})^{0.32} = \frac{24}{Re_m}(1+0.325Re_m^{0.474}) \quad (41)$$

$$Nu_{film}(1+B_{H,film})^{0.7} = 2+0.454Re_m^{0.615}Pr_{film}^{0.98} \quad (42)$$

for $0.4 \leqslant B_{H,film} \leqslant 13$; $30 \leqslant Re_m \leqslant 200$.

The correlation of Sherwood number is approximated by

$$Sh_{film}(1+B_{M,film})^{0.557} = 2+0.39Re_m^{0.54}Sc_{film}^{0.76} \quad (43)$$

for $0.2 \leqslant B_{M,film} \leqslant 6.5$; $30 \leqslant Re_m \leqslant 200$.

Our Nusselt and Sherwood correlations show the strong dependency upon Pr_{film} and Sc_{film}, respectively. Pr_{film} in our simulations varied from 0.7 to 1, while Sc_{film} varied from 2.2 to 0.4 throughout the vaporization process.

5. CONCLUDING REMARKS

A numerically efficient and physically accurate algorithm for transient droplet heating and vaporization has been developed. The unsteady Navier–Stokes equations governing a vaporizing droplet in the intermediate Reynolds number flow are solved. Variable properties, surface blowing due to vaporization, internal liquid circulation with transient droplet heating, and droplet deceleration are considered.

The detailed analysis does provide some promising results toward a better understanding of vaporizing droplet behavior. The results indicate that both transient droplet heating and reduction in Reynolds number (largely due to droplet deceleration) are major sources of droplet unsteady behavior and persist during most of the droplet's lifetime. The heat transfer mechanism within the droplet is initially dominated by diffusion. When the internal flow gains strength, the main heat transfer mechanism switches to convection. Finally, the reduction of the surface shear stress causes the internal circulation to decrease, with diffusion again becoming the dominant mechanism. The global results show that the drag coefficient may increase or decrease with time over different portions of the droplet lifetime. The drag coefficient does not simply increase as Reynolds number decreases with time since the drag coefficient depends not only on the Reynolds number but also on the transfer number. The Nusselt and Sherwood numbers follow a gentle decreasing trend as the Reynolds number slowly decreases.

Surface blowing causes the increase of boundary layer thickness as well as reduction of the thermophysical properties at the interface. As a result, the rates of momentum, heat, and mass transfer processes

around the droplet are impeded. This effect is greater for higher effective transfer number cases. The effect of variable properties cannot be neglected for the large temperature difference from the droplet surface to the far stream environment; otherwise, the global results may be seriously overestimated. Preheating the droplet can reduce the drag coefficient significantly due to the enhanced surface blowing effect. Different initial Reynolds numbers may result in quite different drag coefficients during the early times; however, the drag coefficients asymptotically reach a certain form which is dominated by current values of the Reynolds number. The rapid mixing droplet model can overestimate the drag coefficient due to the improper consideration of the rate of droplet heating.

From an ample amount of numerical data, one set of reasonably accurate correlations has been obtained for drag coefficients and Nusselt and Sherwood numbers.

Acknowledgements—This work has been supported by the Air Force Office of Scientific Research under Grant No. 86-0016-D with Dr Julian Tishkoff acting as the technical monitor. The support of the San Diego Supercomputer Center is greatly appreciated.

REFERENCES

1. R. Clift, J. R. Grace and M. E. Weber, *Bubbles, Drops, and Particles*. Academic Press, New York (1978).
2. C. K. Law, Unsteady droplet vaporization with droplet heating, *Combustion Flame* **26,** 17–22 (February 1976).
3. C. K. Law and W. A. Sirignano, Unsteady droplet combustion with droplet heating. II. Conduction limit, *Combustion Flame* **29,** 175–186 (March 1977).
4. W. A. Sirignano, Theory of multi-component fuel droplet vaporization, *Arch. Thermodyn. Combust.* **9**(2), 231 247 (1978).
5. S. Prakash and W. A. Sirignano, Theory of convective droplet vaporization with unsteady heat transfer in the circulating liquid phase, *Int. J. Heat Mass Transfer* **23,** 253–268 (1980).
6. P. Lara-Urbaneja and W. A. Sirignano, Theory of transient multicomponent droplet vaporization in a convective field, *Eighteenth Symp. (Int.) on Combustion*, pp. 1365–1374. Combustion Institute, Pittsburgh, Pennsylvania (1981).
7. A. Y. Tong and W. A. Sirignano, Analytical solution for diffusion and circulation in a vaporizing droplet, *Nineteenth Symp. (Int.) on Combustion*, pp. 1007–1020. Combustion Institute, Pittsburgh, Pennsylvania (1982).
8. W. A. Sirignano, Fuel droplet vaporization and spray combustion theory, *Prog. Energy Combust. Sci.* **9,** 291–322 (1983).
9. H. A. Dwyer and B. R. Sanders, Detailed computation of unsteady droplet dynamics, *Twentieth Symp. (Int.) on Combustion*, pp. 1743 1749. Combustion Institute, Pittsburgh, Pennsylvania (1984).
10. H. A. Dwyer and B. R. Sanders, Comparative study of droplet heating and vaporization at high Reynolds and Peclet numbers, *Dynamics of Flames and Reactive Systems, AIAA Progress in Astronautics*, Vol. 95, pp. 464–483 (1984).
11. H. A. Dwyer and B. R. Sanders, Droplet dynamics and vaporization with pressure as a parameter, *ASME Winter Annual Meeting*, Paper 84-WA/HT-20 (1984).
12. G. Patnaik, W. A. Sirignano, H. A. Dwyer and B. R. Sanders, A numerical technique for the solution of a vaporizing fuel droplet, *Prog. Astronaut. Aeronaut.* **105,** 253–266 (1986).
13. J. N. Chung, P. S. Ayyaswamy and S. S. Sadhal, Laminar condensation on a moving drop. Part 1. Singular perturbation technique, *J. Fluid Mech.* **139,** 105–130 (1984).
14. J. N. Chung, P. S. Ayyaswamy and S. S. Sadhal, Laminar condensation on a moving drop. Part 2. Numerical solutions, *J. Fluid Mech.* **139,** 131–144 (1984).
15. T. Sundararajan and P. S. Ayyaswamy, Hydrodynamics and heat transfer associated with condensation on a moving drop: solutions for intermediate Reynolds numbers, *J. Fluid Mech.* **149,** 33–58 (1984).
16. R. J. Haywood, N. Nafziger and M. Renksizbulut, A detailed examination of gas and liquid phase transient processes in convective droplet evaporation, *J. Heat Transfer* **111,** 495–502 (1989).
17. M. Vinokur, Conservation equations of gas-dynamics in curvilinear coordinate systems, *J. Comput. Phys.* **14,** 105–125 (1974).
18. G. Ryskin and L. G. Leal, Numerical solution of free-boundary problems in fluid mechanics. Part 1. The finite-difference technique, *J. Fluid Mech.* **148,** 1–17 (1984).
19. N. B. Vargaftik, *Tables on the Thermophysical Properties of Liquids and Gases*. Hemisphere, Washington, DC (1975).
20. B. Abramzon and W. A. Sirignano, Droplet vaporization model for spray combustion calculations, *Int. J. Heat Mass Transfer* **32,** 1605–1618 (1989).
21. C. K. Westbrook, A generalized ICE method for chemically reactive flows in combustion systems, *J. Comput. Sci.* **29,** 67–80 (1978).
22. G. Patnaik, A numerical solution of droplet vaporization with convection, Ph.D. Dissertation, Carnegie-Mellon University, Department of Mechanical Engineering (1986).

ANALYSE NUMERIQUE D'UNE GOUTTELETTE DE CARBURANT A PROPRIETES VARIABLES QUI CONVECTE ET S'EVAPORE

Résumé—L'analyse détaillée d'une gouttelette de carburant froid est étudiée après l'injection dans un courant de gaz chaud. On considère les effets des propriétés variables, du chauffage variable et de la circulation interne du liquide, de la décélération de l'écoulement par la trainée de la gouttelette, du soufflage de la couche limite et de l'interface mobile. Plusieurs études paramétriques sont traitées en changeant les grandeurs suivantes: température initiale de la goutte, température ambiante, nombre de Reynolds initial, type de carburant et modèle de chauffage de la gouttelette. Les résultats montrent que pour des nombres élevés de transfert, la vitesse de vaporisation est grande et le coefficient de trainée est significativement réduit, principalement à cause de la forte réduction de la force de frottement. Pour des plus faibles nombres de transfert, l'effet du soufflage de la couche-limite est plus faible et le coefficient de trainée est dominé par le nombre de Reynolds.

NUMERISCHE UNTERSUCHUNG VON BEWEGLICHEN VERDAMPFENDEN KRAFTSOFFTRÖPFCHEN MIT VARIABLEN STOFFEIGENSCHAFTEN

Zusammenfassung—In der vorliegenden Arbeit werden die Vorgänge in einem kalten Kraftstofftröpfchen eingehend untersucht, das plötzlich in einen heißen Gasstrom injiziert wird. Dabei werden die Einflüsse variabler thermophysikalischer Stoffeigenschaften berücksichtigt, außerdem die transiente Wärmezufuhr und innere Zirkulation der Flüssigkeit, die Verzögerung der Strömung aufgrund des Tröpfchenwiderstandes, das Wegblasen der Grenzschicht und die bewegliche Grenzfläche. Folgende Parameter werden systematisch variiert: Anfängliche Tropfentemperatur, Umgebungstemperatur, anfängliche Reynolds-Zahl, Art des Kraftstoffs und Beheizungsmodell für das Tröpfchen. Die Ergebnisse zeigen, daß bei größeren Kennzahlen für den Wärmeübergang stärkere Verdunstung auftritt; der Widerstandsbeiwert wird signifikant kleiner, was im wesentlichen auf eine starke Verringerung der Reibung zurückzuführen ist. Bei kleinen Kennzahlen für den Wärmeübergang ist der Grenzschichteffekt geringer und der Widerstandsbeiwert wird allein von der Reynolds-Zahl beeinflußt. Die Ergebnisse zeigen auch, daß sich bei konstanten Stoffeigenschaften ein zu großer Widerstandsbeiwert ergeben würde.

ЧИСЛЕННЫЙ АНАЛИЗ КАПЛИ ТОПЛИВА С ПЕРЕМЕННЫМИ СВОЙСТВАМИ В ПРОЦЕССЕ КОНВЕКЦИИ И ИСПАРЕНИЯ

Аннотация—Дан детальный анализ характеристик капли ненагретого топлива, мгновенно впрыскиваемого в поток нагретого газа. Учитываются эффекты изменяющихся теплофизических свойств, нестационарного нагрева и внутренней циркуляции жидкости, снижения скорости течения за счет сопротивления капли, вдува в пограничный слой, а также движущейся границы раздела. Проведено несколько параметрических исследований, при которых варьировались такие величины, как начальная температура капли, температура окружающей среды, исходное число Рейнольдса, вид топлива, а также модель нагрева капли. Полученные результаты показывают, что при высоких числах переноса интенсивность испарения возрастает и коэффициент сопротивления существенно уменьшается главным образом благодаря значительному сокращению сопротивления трения. В случае низких чисел переноса влияние вдува в пограничный слой является более слабым и коэффициент сопротивления определяется числом Рейнольдса.